



Unconventional Fermi surface spin textures in the $\text{Bi}_x\text{Pb}_{1-x}/\text{Ag}(111)$ surface alloy

Fabian Meier,^{1,2} Vladimir Petrov,³ Sebastian Guerrero,⁴ Christopher Mudry,⁴ Luc Patthey,² Jürg Osterwalder,¹ and J. Hugo Dil^{1,2}

¹Physik-Institut, Universität Zürich, Winterthurerstrasse 190, CH-8057 Zürich, Switzerland

²Swiss Light Source, Paul Scherrer Institut, CH-5232 Villigen, Switzerland

³St. Petersburg Polytechnical University, 29 Polytechnicheskaya Street, 195251 St. Petersburg, Russia

⁴Condensed Matter Theory Group, Paul Scherrer Institut, CH-5232 Villigen, Switzerland

(Received 27 February 2009; revised manuscript received 17 April 2009; published 30 June 2009)

The Fermi and Rashba energies of surface states in the $\text{Bi}_x\text{Pb}_{1-x}/\text{Ag}(111)$ alloy can be tuned simultaneously by changing the composition parameter x . We report on unconventional Fermi surface spin textures observed by spin and angle-resolved photoemission spectroscopy that are correlated with a topological transition of the Fermi surface occurring at $x=0.5$. We show that the surface states remain fully spin polarized upon alloying and that the spin-polarization vectors are approximately tangential to the constant energy contours. We discuss the implications of the topological transition for the transport of spin.

DOI: 10.1103/PhysRevB.79.241408

PACS number(s): 73.20.At, 71.70.Ej, 79.60.-i

Controlling the spin degree of freedom of the electron lies at the heart of spintronics.¹ One possibility of manipulating the electron spin without the need of any external magnetic field is found in the Rashba-Bychkov (RB) effect.² It appears in (quasi-)two-dimensional electron or hole systems with a lack of inversion symmetry and plays a prominent role for a proposed spin field-effect transistor.³ For most systems, the RB effect is small. Therefore, many of the related intriguing effects, such as a renormalization of the Fermi-liquid parameters,⁴ changes in the electron-phonon coupling,⁵ enhanced superconductivity transition temperatures,⁶ and real-space-spin accumulation,⁷⁻⁹ remain for the most part experimentally unobservable.

Recently, it has been shown that the RB effect is dramatically enhanced in the $\text{Bi}/\text{Ag}(111)(\sqrt{3}\times\sqrt{3})R30^\circ$ and $\text{Pb}/\text{Ag}(111)(\sqrt{3}\times\sqrt{3})R30^\circ$ surface alloys due to an additional in-plane inversion asymmetry.¹⁰⁻¹⁴ Furthermore, the band structure can be continuously tuned between these two systems by substituting Bi with Pb,¹⁵ as schematically illustrated in Fig. 1(a). The large RB effect combined with the tunability of the Fermi and the RB energies make $\text{Bi}_x\text{Pb}_{1-x}/\text{Ag}(111)(\sqrt{3}\times\sqrt{3})R30^\circ$, henceforth $\text{Bi}_x\text{Pb}_{1-x}/\text{Ag}(111)$, an ideal model RB system to study the geometrical and the topological changes in the Fermi surface of its surface states.^{5,16} It is clear that the large conductivity of the Ag substrate short-circuits possible spin currents at the surface of $\text{Bi}_x\text{Pb}_{1-x}/\text{Ag}(111)$, but RB semiconductors¹⁷ or thin metallic films¹⁸ might be found that are equally tunable and suited for technological applications. In this context it is of importance to study the effect of random intermixing on the spin structure of RB systems.

We present in this work spin and angle-resolved photoemission spectroscopy (SARPES) data on surface states of $\text{Bi}_x\text{Pb}_{1-x}/\text{Ag}(111)$ to resolve the changes in their Fermi surface spin textures (FSSTs) as a function of composition x . We will argue that the spin transport is strongly affected by a topological transition of the Fermi surface taking place at the critical value $x_c \approx 0.5$.

The RB effect occurs at interfaces or surfaces whenever the absence of the space inversion symmetry lifts the spin degeneracy due to the spin-orbit coupling. The simplest example of a RB Hamiltonian is given by¹⁹

$$H = H_0 + H_{\text{RB}}, \quad (1a)$$

where the kinetic energy of the two-dimensional hole gas with negative effective mass m^* is

$$H_0 = \sigma_0 \left(E_{\bar{\Gamma}} - \frac{\hbar^2}{2m^*} \nabla^2 \right), \quad (1b)$$

while the RB term is

$$H_{\text{RB}} = -\alpha_{\text{RB}} \left(i\sigma_y \frac{\partial}{\partial x} - i\sigma_x \frac{\partial}{\partial y} \right). \quad (1c)$$

The positive coupling constant α_{RB} reflects the RB coupling. The unit 2×2 matrix is denoted by σ_0 , while σ_x and σ_y are the standard Pauli matrices in the basis in which the quantization axis is along the z direction. The eigenenergies of H yield the upper (+) and lower (-) RB branches

$$E_{\pm}(\mathbf{k}) = E_{\bar{\Gamma}} + \frac{\hbar^2 |\mathbf{k}|^2}{2m^*} \pm \alpha_{\text{RB}} |\mathbf{k}|. \quad (2a)$$

The corresponding eigenspinors are

$$\langle \mathbf{k}, \pm | = (e^{i(\varphi \pm \pi/2)}, 1) / \sqrt{2}, \quad (2b)$$

where $\varphi = \arctan(k_y/k_x)$ and the two-dimensional momentum \mathbf{k} is measured relative to the $\bar{\Gamma}$ point. Although H_{RB} breaks the spin-rotation symmetry of H_0 , it preserves time-reversal symmetry and the system remains nonmagnetic. The mechanism of the enhanced spin splitting in the $\text{Bi}_x\text{Pb}_{1-x}/\text{Ag}(111)$ surface alloy goes beyond this simple model. Nevertheless, many of the fundamental properties of this system are captured by the simple nearly-free-electron RB model.

We plot in Fig. 1(b) the dispersion of the nearly-free-electron RB model. The dispersion along any cut passing through the $\bar{\Gamma}$ point can be assigned two distinct colors that distinguish the antiparallel alignments of the spin expectation values for the eigenspinors. This gives two spin-split bands colored in blue (dark gray) and red (light gray) in Fig. 1(b). They are offset by two opposite wave vectors of magnitude k_0 when measured from $\bar{\Gamma}$. The Rashba energy $E_R = \hbar^2 k_0^2 / (2|m^*|)$ is defined as the difference between apex and

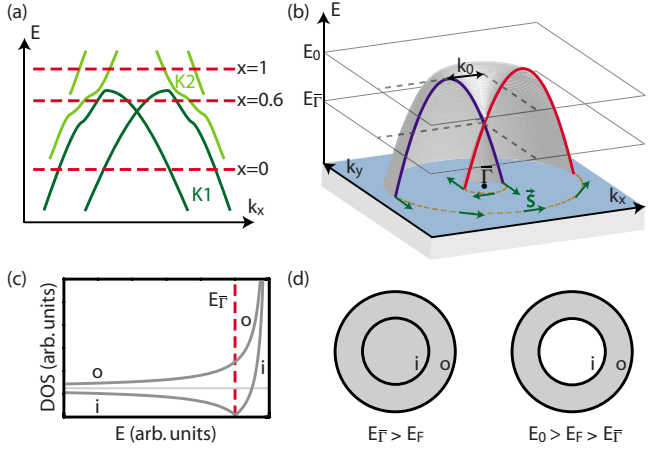


FIG. 1. (Color online) (a) Qualitative plot of the surface-state band structure of Bi/Ag(111) ($x=1$) along the direction $\bar{\Gamma}\bar{K}$ in momentum space (adapted from Ref. 13) showing the two Kramer's pairs K1 and K2. As x is decreased, the Fermi level (dashed lines) lowers continuously and the spin splitting becomes smaller (not shown). (b) Schematic picture of the Rashba effect for a two-dimensional hole gas around $\bar{\Gamma}$ and illustration of the relevant parameters. The green (dark gray) arrows are the spin expectation values of the eigenspinors. (c) Density of states for the outer (o) and inner (i) constant energy contours. (d) Hole Fermi seas (gray regions) and Fermi surfaces (thick lines) when $E_{\bar{\Gamma}} > E_F$ and $E_0 > E_F > E_{\bar{\Gamma}}$.

crossing point of the Kramer's pair. The spin-polarization vectors $S_{\pm}(\mathbf{k})$, defined as the spin expectation values of the eigenspinors $|\mathbf{k}, \pm\rangle$, are parallel to the basal plane of Fig. 1 and are orthogonal to \mathbf{k} , as depicted by the green (dark gray) arrows in Fig. 1(b). Below $E_{\bar{\Gamma}}$, the spin polarization rotates counterclockwise along the outer constant energy contour and clockwise for the inner contour. Above $E_{\bar{\Gamma}}$, the spin polarization rotates counterclockwise along both contours. The experimentally determined spin-polarization vectors are denoted by $\mathbf{P}=(P_x, P_y, P_z)$ and will be shown to obey this simple rule.

The density of states (DOS) $\nu(E_F)$ of the Hamiltonian defined in Eq. (1) is also sensitive to the change in the geometry and topology of the Fermi surface upon tuning of the Fermi energy E_F . The DOS $\nu_{o,i}(E_F)$ of the outer (o) and the inner (i) Fermi contour shown in Fig. 1(c) are given by

$$\nu_{o,i}(E_F) = \Theta(E_0 - E_F) \nu_{2D} \left| 1 \pm \sqrt{\frac{E_0 - E_{\bar{\Gamma}}}{E_0 - E_F}} \right|, \quad (3)$$

whereby Θ is the Heaviside function and $\nu_{2D} = |m^*| / (2\pi\hbar^2)$. The + refers to the outer Fermi contour and the - to the inner one. The sum $\nu_o(E_F) + \nu_i(E_F)$ reduces to the constant DOS $2\nu_{2D}$ of a spin-degenerate two-dimensional hole gas with parabolic dispersion when $E_{\bar{\Gamma}} > E_F$, has a singular derivative when $E_F = E_{\bar{\Gamma}}$, while it displays the one-dimensional Van Hove singularity $\nu(E_F) \sim (E_0 - E_F)^{-1/2}$ in the limit $E_F \rightarrow E_0$.

The $\text{Bi}_x\text{Pb}_{1-x}/\text{Ag}(111)$ sample preparation was carried out *in situ* under ultrahigh vacuum conditions with a base pressure better than 2×10^{-10} mbar. The Ag(111) crystal was cleaned by multiple cycles of Ar^+ sputtering and annealing.

Bi and Pb were simultaneously deposited from a calibrated evaporator at a pressure below 4×10^{-10} mbar, with the total amount corresponding to 1/3 of a monolayer. During deposition, the sample was held at elevated temperatures ($T \approx 200$ °C). The sample quality was affirmed by low-energy electron diffraction, which showed sharp $(\sqrt{3} \times \sqrt{3})R30^\circ$ spots and no further superstructure, and angle-resolved photoemission spectroscopy (ARPES), which showed a continuous tuning of the band structure and no superposition of the Bi/Ag(111) and the Pb/Ag(111) band structures. These are both strong indications that, although the surface is well ordered, Bi and Pb are randomly substituted.

The experiments were performed at room temperature at the Surface and Interface Spectroscopy beamline at the Swiss Light Source of the Paul Scherrer Institute using the COPHEE spectrometer.²⁰ The data were obtained using horizontally polarized light with a photon energy of 24 eV, where the intensity distribution is most symmetric. There is a 45° angle between the incoming photons and the measured electrons, which defines the xz plane. A momentum distribution curve (MDC) is taken along the k_x axis (corresponding to a sample rotation around the y axis). This means that a spin-polarization vector \mathbf{P} is expected to point in the $\pm y$ direction if the nearly-free-electron RB model holds qualitatively. Because of the inherently low efficiency of Mott detectors the energy and angular resolution were sacrificed in the spin-resolved measurements up to 80 meV and 1.5° , respectively.

A detailed description of the band structure of Bi/Ag(111) and Pb/Ag(111) can be found in Refs. 10–12. There are two Kramer's pairs K1 and K2 of bands that are qualitatively drawn in Fig. 1(a). The inner one (K1) is mostly of sp_z symmetry. The outer one (K2) is mostly of $p_{x,y}$ symmetry. For Pb/Ag(111) ($x=0$), both K1 and K2 are only partially occupied. For Bi/Ag(111) ($x=1$), K1 is fully occupied, while K2 is only partially occupied. Irrespective of $x=0$ or $x=1$, the spin-polarization vectors for K1 are nearly parallel to the surface plane and are approximately perpendicular to the momenta, in agreement with our model. In contrast, the spin-polarization vectors for K2 feature significant out-of-plane components depending on the crystallographic direction. This is a consequence of the stronger coupling to in-plane potential gradients.^{10,12} We will only consider K1 from now on.

Figure 2 shows the experimental band structure of the $\text{Bi}_x\text{Pb}_{1-x}/\text{Ag}(111)$ surface alloys along $\bar{\Gamma}\bar{K}$ for $x=0.5, 0.6$, and 1 measured with (spin integrated) ARPES. Second derivative data are also shown to enhance the contrast. The band K1 is fully occupied for $x=1$ and, as x is decreased, the Fermi level shifts down with respect to the bands so that K1 gets depopulated, and the spin splitting decreases. For $x=0.6$, the Fermi level E_F lies between the band apex and the crossing point ($E_0 > E_F > E_{\bar{\Gamma}}$), where unconventional FSST are expected. At $x=0.5$, the Fermi level lies approximately at the crossing point of K1, where the DOS of the inner Fermi contour vanishes and a topological transition of the Fermi surface occurs. Note that our calibration of x is slightly different from that given in Ref. 15. However, this does not affect the conclusions of this work.

We show in Fig. 3 the experimental spin-resolved MDCs

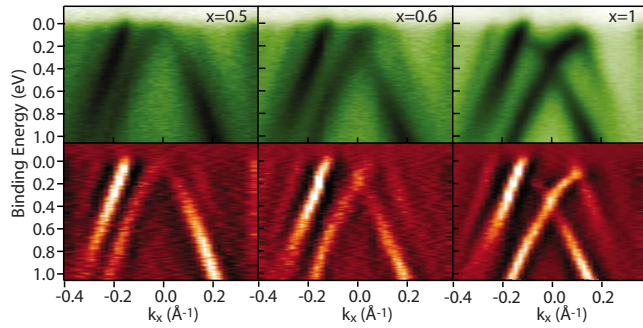


FIG. 2. (Color online) Upper graphs: experimental band structure of $\text{Bi}_x\text{Pb}_{1-x}/\text{Ag}(111)$ for $x=0.5, 0.6,$ and 1 (from left to right) along the $\bar{\Gamma}\bar{K}$ direction, where dark corresponds to a higher photoemission intensity. Lower graphs: second derivative data to enhance the contrast.

for $x=0.5$ (left column) and $x=0.6$ (right column) providing us with the FSST for $E_{\bar{\Gamma}} > E_F$ and $E_0 > E_F > E_{\bar{\Gamma}}$, respectively. The extraction of the spin-polarization vectors \mathbf{P} was done by applying a two-step fitting routine¹² on the data of Fig. 3. For both compositions, we find that the surface states $K1$ remain fully spin polarized with spin-polarization vectors similar to those of the surface states of $\text{Bi}/\text{Ag}(111)$ or $\text{Pb}/\text{Ag}(111)$ found in Ref. 12. The spin-polarization vectors lie mainly in the surface plane perpendicular to \mathbf{k} and both the out-of-plane and radial spin-polarization components are comparatively small. This finding is corroborated by several similar measurements in different crystallographic directions and at different binding energies. We thus conclude that the spin polarization of the surface states $K1$ is robust against the mixing of Bi and Pb.

For $x=0.5$, the measurement is performed slightly below the crossing point of $K1$. We observe the conventional situation, i.e., a straight cut from $\bar{\Gamma}$ to the surface Brillouin-zone (SBZ) boundary crosses two bands with opposite spin-polarization vectors. This can be seen in the spin-resolved spectra of Fig. 3(a), which are obtained from the fits of the corresponding spin-polarization data shown in Fig. 3(c). The

spin-polarization vectors of the bands are opposite for all adjacent bands. The corresponding qualitative FSST are drawn in the inset of Fig. 3(c).

For $x=0.6$, an unconventional FSST is observed. Fitting the spin-polarization data of Fig. 3(d) clearly shows that, for positive and negative k_x , both bands crossing the Fermi energy have nearly parallel spin-polarization vectors. The corresponding spin-resolved spectra are displayed in Fig. 3(b). Due to strong transition matrix element effects, the inner band on the left side of normal emission is only visible as a weak shoulder of the $I_{y,dn}$ curve. When $E_0 > E_F > E_{\bar{\Gamma}}$, the FSST match qualitatively those shown in the inset of Fig. 3(d). A cut from $\bar{\Gamma}$ to the SBZ boundary crosses two bands with parallel spin-polarization vectors.

We have thus established that varying x between 0.5 and 0.6 induces a topological transition in the shape of the Fermi surface of $K1$ surface states with an impact on their spin texture and on their DOS that is qualitatively captured by the nearly-free-electron RB model. We will now argue that the transport of spins across an ideal one-dimensional boundary separating a spin-degenerate two-dimensional electron gas from a RB hole gas is sensitive to this topological transition.

In principle, a two-dimensional scattering geometry, as depicted in Fig. 4(a), could be realized by the deposition of $\text{Bi}_x\text{Pb}_{1-x}$ on $\text{Ag}(111)$ through a shadow mask. We denote with x and y the coordinates of the two-dimensional $\text{Ag}(111)$ surface. A spin-degenerate electron gas with an effective mass corresponding to that of $\text{Ag}(111)$ surface states meets the states from the $K1$ band of $\text{Bi}_x\text{Pb}_{1-x}/\text{Ag}(111)$ at the ideal one-dimensional boundary $x=0$. We imagine driving a small charge current through the boundary by applying an infinitesimal voltage difference across the interface. The polarity of this applied voltage defines whether the charge current is from the left to the right, i.e., from the $\text{Ag}(111)$ to the RB side, or from the right to the left, i.e., from the RB to the $\text{Ag}(111)$ side. In the Drude limit, the charge current can be calculated from the reflection coefficients R_σ for an incoming surface state of energy E_F with spin quantum number σ along some quantization axis, which is here chosen to be the y axis.

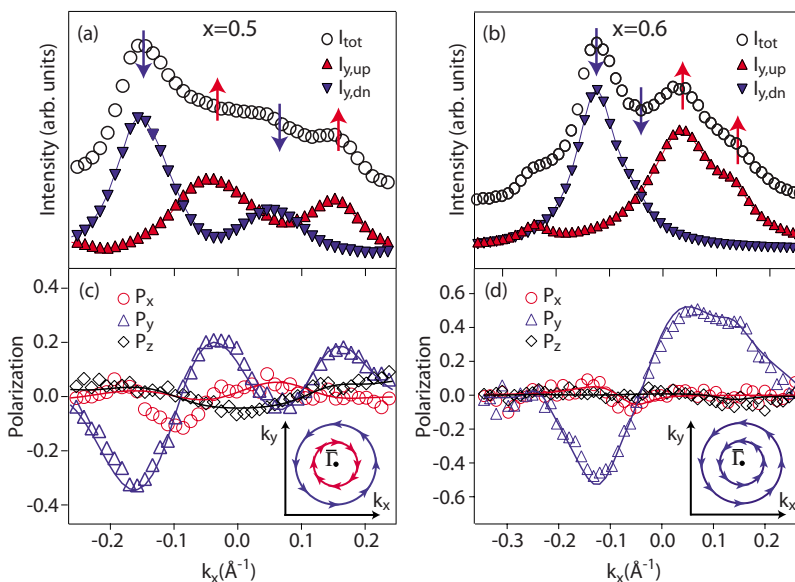


FIG. 3. (Color online) Spin resolved ARPES data of $\text{Bi}_x\text{Pb}_{1-x}/\text{Ag}(111)$ for $x=0.5$ (left) and $x=0.6$ (right) measured at a binding energy of 50 meV. (a) and (b) Total spin integrated intensity (circles) and spin-resolved intensity curves projected on the y axis of a MDC along $\bar{\Gamma}\bar{K}$. (c) and (d) are the corresponding measured (symbols) and fitted (solid lines) spin-polarization data. (Insets) Schematically drawn FSST. For $x=0.6$, both bands of $K1$ crossing E_F between $\bar{\Gamma}$ and the SBZ boundary have parallel spin-polarization vectors, while for $x=0.5$, the spin-polarization vectors are antiparallel.

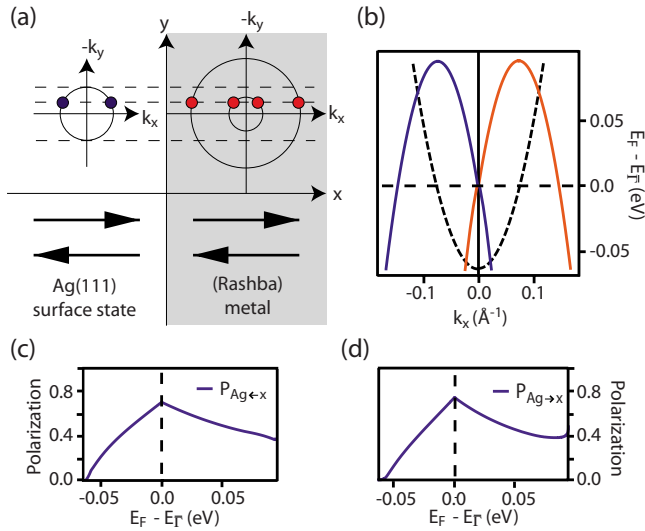


FIG. 4. (Color online) (a) Incoming and outgoing surface plane waves from the interface at $x=0$ between a spin isotropic ($x < 0$) and a RB ($x > 0$) metal. (b) Dispersions of the Ag(111) (dashed line) and RB (solid lines) surface states. (c) $P_{\text{Ag} \leftarrow x}$ and (d) $P_{\text{Ag} \rightarrow x}$ as a function of $E_F - E_{\Gamma}$ as defined in the text.

We denote the spin current by $P_{\text{Ag} \rightarrow x}$ when the current is from the Ag(111) to the RB side or by $P_{\text{Ag} \leftarrow x}$ otherwise. To quantify the transport of spin across the boundary, we divide, on the Ag(111) side, the spin current normal to the boundary (the difference between the spin-up and spin-down currents) by the particle current normal to the boundary, i.e., $P_{\text{Ag} \leftrightarrow x} = (j_{\text{up}} - j_{\text{dn}}) / j_{\text{tot}}$. We use the parameters $m_{\text{Ag}}^* / m_e = 0.397$ and $E_{\Gamma, \text{Ag}} = -63$ meV on the Ag(111) side²¹ and $m_x^* / m_e = -0.25$, $E_{0,x} = 94$ meV, $E_{\Gamma,x} = 0$, on the RB side.¹⁵ The Ag(111) and RB dispersions are shown in Fig. 4(b).

We plot in Fig. 4(c) $P_{\text{Ag} \leftarrow x}$, and in Fig. 4(d) $P_{\text{Ag} \rightarrow x}$ for different band fillings as described by the value of E_F (see Ref. 22 for computational details). In the absence of RB coupling, the spin current across the boundary vanishes. The breaking of the spin-rotation symmetry by the RB coupling induces a spin current on the Ag(111) side in Figs. 4(c) and 4(d). This induced spin current is strongly enhanced by the onset of an unconventional FSST when the Fermi level triggers a topological transition of the RB Fermi surface and ν_1 vanishes. Thus, the RB metal acts as a spin injector or a spin acceptor depending on the polarity of the applied voltage difference across the boundary. Finally, even for nonideal systems, such spin currents might lead to local spin accumulation that could be detected with magnetic scanning tunneling microscopy.

In conclusion, we have measured with SARPES two different types of Fermi surface spin textures in the $\text{Bi}_x\text{Pb}_{1-x}/\text{Ag}(111)$ surface alloys. They are separated at $x \approx 0.5$ by a topological transition in the Fermi surface. In the conventional situation $x < 0.5$, the spin polarizations on the two RB-split Fermi contours rotate in opposite directions. In the unconventional situation $0.5 < x < 0.7$, they rotate in the same direction. Despite the random intermixing of Bi and Pb, the measured momentum-resolved spin polarizations are well reproduced by a phenomenological disorder-free nearly-free-electron RB model in which x merely tunes the Fermi energy and the curvature of the Fermi sea. At last, we have argued that RB-like systems with strong spin-orbit splitting and $E_F \approx E_{\Gamma}$ can be used as a spin filter and thus can lead to a finite spin accumulation in nonmagnetic materials without the need of any magnetic field.

Fruitful discussions with M. Grioni and G. Bihlmayer are gratefully acknowledged. We thank C. Hess, F. Dubi, and M. Klöckner for technical support. This work is supported by the Swiss National Science Foundation.

¹S. A. Wolf *et al.*, *Science* **294**, 1488 (2001).

²Y. A. Bychkov and E. I. Rashba, *JETP Lett.* **39**, 78 (1984).

³S. Datta and B. Das, *Appl. Phys. Lett.* **56**, 665 (1990).

⁴D. S. Saraga and D. Loss, *Phys. Rev. B* **72**, 195319 (2005).

⁵E. Cappelluti, C. Grimaldi, and F. Marsiglio, *Phys. Rev. B* **76**, 085334 (2007).

⁶E. Cappelluti, C. Grimaldi, and F. Marsiglio, *Phys. Rev. Lett.* **98**, 167002 (2007).

⁷J. Sinova *et al.*, *Phys. Rev. Lett.* **92**, 126603 (2004).

⁸J. Wunderlich, B. Kaestner, J. Sinova, and T. Jungwirth, *Phys. Rev. Lett.* **94**, 047204 (2005).

⁹M.-H. Liu, G. Bihlmayer, S. Blügel, and C.-R. Chang, *Phys. Rev. B* **76**, 121301(R) (2007).

¹⁰C. R. Ast *et al.*, *Phys. Rev. Lett.* **98**, 186807 (2007).

¹¹D. Pacilé *et al.*, *Phys. Rev. B* **73**, 245429 (2006).

¹²F. Meier, H. Dil, J. Lobo-Checa, L. Patthey, and J. Osterwalder, *Phys. Rev. B* **77**, 165431 (2008).

¹³G. Bihlmayer, S. Blügel, and E. V. Chulkov, *Phys. Rev. B* **75**, 195414 (2007).

¹⁴J. Prempfer, M. Trautmann, J. Henk, and P. Bruno, *Phys. Rev. B* **76**, 073310 (2007).

¹⁵C. R. Ast *et al.*, *Phys. Rev. B* **77**, 081407(R) (2008).

¹⁶C. R. Ast, G. Wittich, P. Wahl, R. Vogelgesang, D. Pacilé, M. C. Falub, L. Moreschini, M. Papagno, M. Grioni, and K. Kern, *Phys. Rev. B* **75**, 201401(R) (2007).

¹⁷J. Nitta, T. Akazaki, H. Takayanagi, and T. Enoki, *Phys. Rev. Lett.* **78**, 1335 (1997).

¹⁸J. H. Dil *et al.*, *Phys. Rev. Lett.* **101**, 266802 (2008).

¹⁹R. Winkler, *Spin-Orbit Coupling Effects in Two-Dimensional Electron and Hole Systems*, Springer Tracts in Modern Physics (Springer, Berlin, 2003), Vol. 191.

²⁰M. Hoesch, T. Greber, V. N. Petrov, M. Muntwiler, M. Hengsberger, W. Auwaerter, and J. Osterwalder, *J. Electron Spectrosc. Relat. Phenom.* **124**, 263 (2002).

²¹F. Reinert, G. Nicolay, S. Schmidt, D. Ehm, and S. Hüfner, *Phys. Rev. B* **63**, 115415 (2001).

²²B. Srisongmuang, P. Pairor, and M. Berciu, *Phys. Rev. B* **78**, 155317 (2008).